

Evaluation of the formation and protectiveness of a lithium-based conversion layer using electrochemical noise

Li, Ziyu; Homborg, Axel; Gonzalez-Garcia, Yaiza; Kosari, Ali; Visser, Peter; Mol, Arjan

DOI

[10.1016/j.electacta.2022.140733](https://doi.org/10.1016/j.electacta.2022.140733)

Publication date

2022

Document Version

Final published version

Published in

Electrochimica Acta

Citation (APA)

Li, Z., Homborg, A., Gonzalez-Garcia, Y., Kosari, A., Visser, P., & Mol, A. (2022). Evaluation of the formation and protectiveness of a lithium-based conversion layer using electrochemical noise. *Electrochimica Acta*, 426, Article 140733. <https://doi.org/10.1016/j.electacta.2022.140733>

Important note

To cite this publication, please use the final published version (if applicable).
Please check the document version above.

Copyright

Other than for strictly personal use, it is not permitted to download, forward or distribute the text or part of it, without the consent of the author(s) and/or copyright holder(s), unless the work is under an open content license such as Creative Commons.

Takedown policy

Please contact us and provide details if you believe this document breaches copyrights.
We will remove access to the work immediately and investigate your claim.



Evaluation of the formation and protectiveness of a lithium-based conversion layer using electrochemical noise

Ziyu Li^a, Axel Homborg^{a,b,*}, Yaiza Gonzalez-Garcia^a, Ali Kosari^a, Peter Visser^c, Arjan Mol^a

^a Department of Materials Science and Engineering, Delft University of Technology, Mekelweg 2, Delft 2628CD, the Netherlands

^b Netherlands Defence Academy, Het Nieuwe Diep 8, Den Helder 1781 AC, the Netherlands

^c AkzoNobel, Rijksweg 31, Sassenheim 2171 AJ, the Netherlands

ARTICLE INFO

Keywords:

Aluminium alloy
Electrochemical noise
Hexavalent chromium replacement
Corrosion inhibition
lithium-based conversion layer

ABSTRACT

The formation process of a lithium-based conversion layer on AA2024-T3 and its corrosion protective behavior are studied using electrochemical noise (EN). Wavelet transform, as well as noise resistance analysis, have been employed to interpret the EN data. The EN data confirmed five different stages during the conversion layer growth, accompanied by anodic dissolution, increasing corrosion protection of the conversion layer, and adsorption, growth and desorption of hydrogen bubbles simultaneously. The detachment of hydrogen bubbles, localized and uniform corrosion generate different features in the EN signals with energy maxima in high, intermediate and low frequency bands, respectively. In addition, EN results show that the lithium-based conversion layer still provides efficient protection after re-immersion in a corrosive environment, even though localized damage occurs. Moreover, the EN data corresponds well with the morphological layer formation and breakdown observed with microscopy techniques. The results demonstrate that EN is a powerful tool to provide continuous time- and frequency-resolved information about inhibition efficiency.

1. Introduction

Aluminium alloys widely applied in the aerospace industry, such as AA2024-T3, are highly susceptible to localized corrosion in aggressive aqueous solutions. The main reason is the inhomogeneous distribution of copper-rich intermetallic particles, significantly improving the alloys' mechanical properties [1–3]. Generally, to extend the service life of aluminium alloys, the use of inhibitors is one of the most common methods for corrosion protection [4–6].

Over the last decades, the most commonly used technologies to enhance the corrosion protection of aluminium alloys are based on hexavalent chromium chemistries, including chromate-based inhibitors and conversion coatings [7]. However, due to the high toxicity and carcinogenicity of these compounds, the REACH Regulation of the European Union has decided to restrict the usage of hexavalent chromium [6]. Currently, many alternative strategies for developing chromate-free inhibitors are proposed. These inhibitors can be divided into several categories, including oxo-anionic, cationic, metal, metal oxide, and organic inhibitors [8]. While several approaches have been reported to achieve promising results, relatively few single or mixed inhibitors exhibit similar protection efficiency compared with

chromate-containing systems [9,10]. Lithium salts have drawn extensive attention for replacing hexavalent-chromium-based corrosion inhibitors due to their robust passivating capability on various aluminium alloys over the recent years [8,11–15]. The earliest report on the passivation function of lithium salts dates back to 1987, when Gui and Devine [16] showed that AA6061-T6 in an alkaline lithium carbonate solution presented passivity under anodic polarization stimulation. Later, Buchheit et al. [17] observed that Li-Al layered double hydroxide (LDH) coatings formed by alkaline lithium salt immersion followed by a low-temperature heat treatment in air or water was capable of providing favourable barrier properties as compared to traditional chromate conversion coatings. The supersaturation of aluminate ions in the solution seems to be an essential step for the formation of the conversion layer. In 2010, Visser and Hayes [18,19] developed a novel coating system where lithium salts are incorporated into organic coatings, serving as a leachable inhibitor to provide active and irreversible corrosion protection.

Morphological and compositional variation of the lithium conversion layer during immersion has been well studied [20,21]. It was revealed that lithium ions are distributed evenly throughout the conversion layer, resulting in a multi-layered structure. The composition of the

* Corresponding author at: Department of Materials Science and Engineering, Delft University of Technology, Mekelweg 2, Delft 2628CD, the Netherlands.

E-mail address: A.M.Homborg@tudelft.nl (A. Homborg).

multi-layered structure varied in the artificial defect in the organic coating due to the differences in the local environment. Usually, the conversion layer consisted of a top columnar layer composed of Li-Al LDH and a dense inner layer composed of an amorphous lithium-containing pseudoboehmite phase [20]. In addition, a porous intermediate layer which contains both amorphous and crystalline compounds may also appear in some local regions inside the defect [20]. To evaluate the lithium-based conversion layer formation on AA2024-T3 in a lithium carbonate solution containing chloride ions, Visser et al. set up an electrochemical cell to mimic the local aqueous environments of a scribed area [14]. Three consecutive stages, including oxide thinning, hydroxide film formation and layer growth were proposed with the additional supporting evidence from compositional and morphological observations.

Moreover, Kosari et al. [22] investigated the local layer formation process with sub-micron resolution at and around intermetallic particles on AA2024-T3. The entire layer formation process (including a columnar outer layer and an inner dense layer out of a 7 h exposure) was divided into five stages. Top-view and cross-sectional observations, supplemented with the recorded open circuit potential (OCP), elucidated the conversion layer formation process consisting of five distinct stages. The entire conversion layer formation process evolves morphologically, compositionally and electrochemically. AA2024-T3 surface does not acquire obvious passivation at stages I and II, during which the passivation is lost and active matrix dissolution, and dealloying of intermetallic particles occurs. The conversion layer formation and growth are mainly associated with the later stages (stage III to stage V). Kosari et al. [22] also found that the passivation process is not synchronized between the aluminium matrix and different intermetallic particles. It was found that the columnar layer formation process on the S-phase preceded that on the aluminium matrix and on other types of intermetallic particles due to the higher electrochemical activity and faster dissolution rate of S-phase, leading to an earlier local supersaturation of aluminate ions and the formation of a columnar layer over the S-phase.

An extensive number of traditional electrochemical techniques like linear polarization resistance (LPR) and electrochemical impedance spectroscopy (EIS) have been applied to evaluate the corrosion protective properties of the lithium-based conversion layer [14,19,23]. However, these measurements only presented electrochemical information at several discrete time points. Therefore, rapid electrochemical reactions might not be identified. In other words, a detailed continuous and time-resolved evolution of electrochemical reactions during the formation process of the lithium-based conversion layer has not been studied and discussed to a large extent yet. Electrochemical noise (EN) is a technique which records a potential and current signal simultaneously and continuously without external perturbation of the system. The capability to monitor rapidly changing electrochemical processes has been reported in prior studies [24–28]. EN has been successfully applied to study conversion layer formation on different metals. For example, Tan et al. [29] investigated the chromate conversion coating (CCC) formation process on aluminium using EN analysis and proved that CCC protection only was established after ageing treatments. Liu et al. [30] studied the *in-situ* formation process in the time and frequency domain of a stannate CC on AZ91D magnesium alloys. It revealed that there were two separate stages including an incubation stage accompanied by the nucleation and nuclei dissolution process, and a periodical growth stage consisting of hemispherical particles growth and dissolution during the CC formation process.

In this paper, EN is applied to investigate the lithium-based conversion layer formation process *in-situ* and continuously, using wavelet transform and noise resistance analysis. In addition, EN was employed to study the irreversibility behavior of the lithium-based conversion layer in a neutral sodium chloride solution.

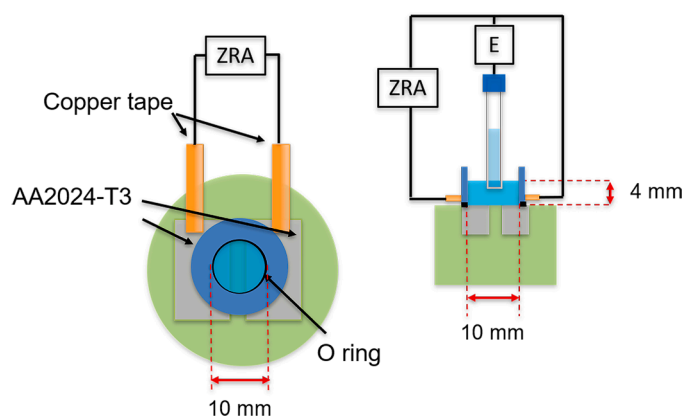


Fig. 1. Layout of the electrochemical cell.

2. Experimental methods

2.1. Materials and experimental set-up

A single commercial bare AA2024-T3 sheet provided by Goodfellow in 0.8 mm thickness served as working electrode material. A commercial pure Al sheet (99.999% purity) of 1 mm thickness was used for control experiments. Two identical specimens with a size of 8 mm × 20 mm were cut out from larger panels. The two samples were embedded in epoxy resin at an interdistance of 2 mm after spraying a primer at four edges to avoid crevice corrosion. Later, the embedded sample was sanded up to grit 4000 with SiC paper and then left in ambient environment for 24 h before the experiments. The pure Al samples were polished on a soft cloth using alumina slurries of 0.5 μm and 0.05 μm after sanding. The adhesive copper tape was connected to both samples separately for electrical connection. In this electrochemical cell, two identical exposed working electrodes were created by covering the working electrode surfaces using a water-proof tape with a round hole of 10 mm diameter. Then an O-ring with a diameter of 10 mm was fitted to the round defect of tape and pressed by a PMMA cell to hold the electrolyte. Laboratory-grade chemicals used in this work were ordered from Sigma-Aldrich (St. Louis, MO, USA).

The measurements were performed in a traditional three-electrode system which contains two identical working electrodes and a saturated Ag/AgCl reference electrode. All measurements were conducted under open circuit potential conditions. In order to mimic the liquid environment on exposed coupons from previous work [22], 321 μL electrolyte containing 0.01 M NaCl and 0.01 M Li₂CO₃ (pH 10.9) was added into the reaction cell to provide a relatively thin film (approx. 4 mm), as illustrated in Fig. 1. Electrolyte containing 0.01 M NaCl and 0.01 M Na₂CO₃ (pH 11.0) was used to compare the behavior of AA2024-T3 in the electrolyte with or without lithium ions.

All experiments were performed in the open air. The exposure duration time for coupons to the electrolyte was 14500s and the room temperature was controlled at 20 °C. A Compactstat from Ivium Technologies was used to record current and potential signals simultaneously, serving as a zero resistance ammeter (ZRA in Fig. 1) and potentiometer (E in Fig. 1). The Compactstat was put into a Faradaic cage to avoid the influence of electromagnetic disturbance caused by external sources. The Compactstat was controlled by a Windows-based PC software. The sampling frequency chosen for this work was 20 Hz and a low-pass filter of 10 Hz was used to avoid aliasing. The EN data were processed using Matlab from MathWorks. Morphological information was obtained using a JEOL JSM-6500F field emission scanning electron microscope (SEM) with the secondary electron detector using an acceleration voltage of 15 kV at a working distance of 10 mm. All experiments were performed at least in triplicate, while the results shown in the supporting document were performed at least two times.

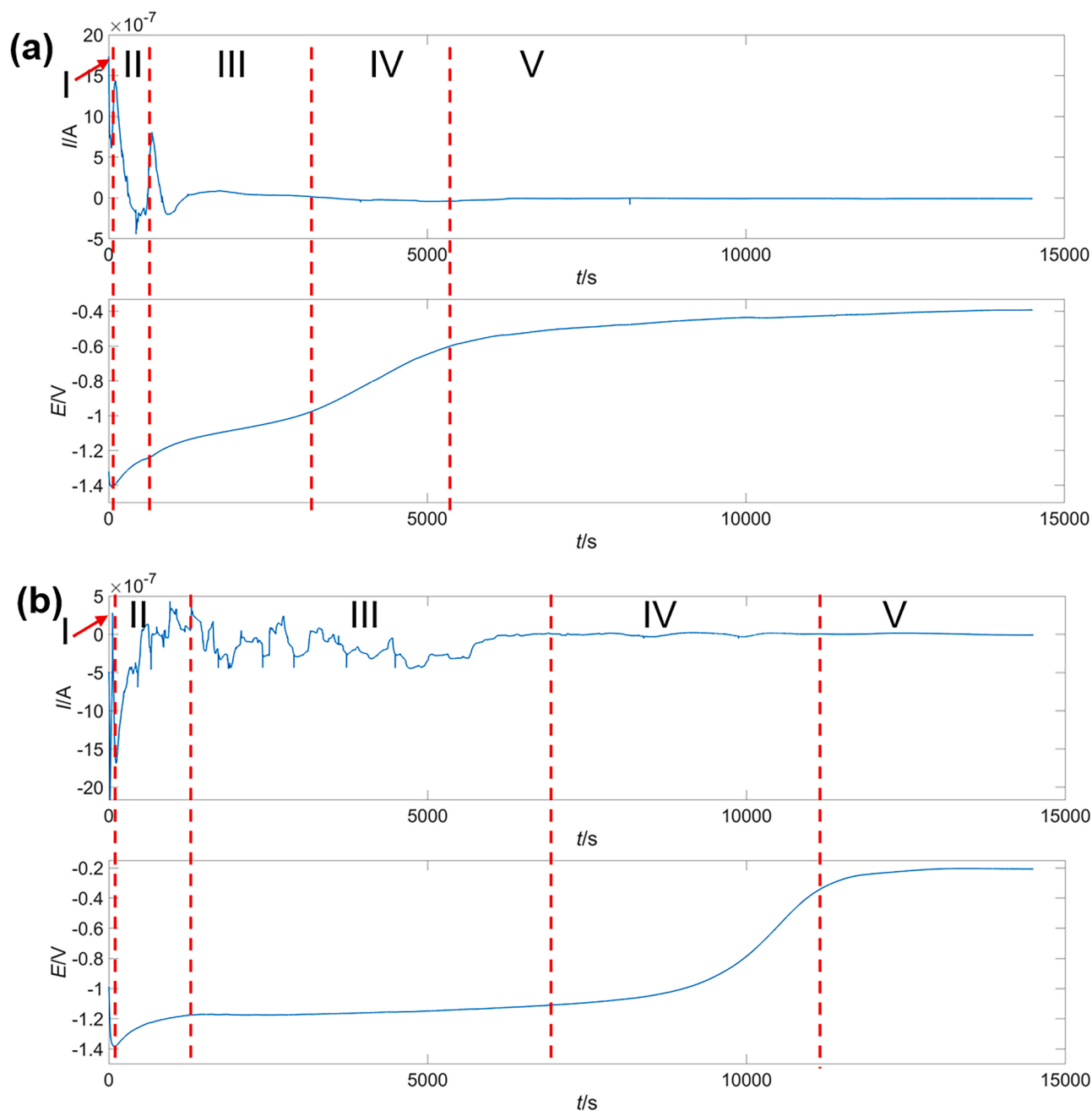


Fig. 2. EN current and potential signal for AA2024-T3 exposed in (a) 0.01 M NaCl and 0.01 M Li_2CO_3 solution, and (b) 0.01 M NaCl and 0.01 M Na_2CO_3 for a duration of 14,500 s.

2.2. EN analysis

Many natural signals are nonstationary and nonlinear, producing a direct current (DC) drift in the raw signals [31]. DC drift is visible as a variation of statistical parameters over time, e.g., a slow alteration of a system under investigation over time. A possible cause of DC drift in the electrochemical current noise could be an increasing asymmetry between working electrodes over the course of a measurement [32,33]. The low frequency contribution generated by DC drift may cause inaccurate and false results on the outcome of data analysis and should be removed prior to further data analysis [31]. There are various methods suitable for this purpose, like moving average, polynomial and linear trend removal, wavelet analysis and empirical mode decomposition [25]. Linear detrending is firstly excluded since this technique is likely to leave behind part of the DC drift. Moving average trend removal

(MAR) is also not highly recommended [34]. Estimating nonuniform drift over longer timeframes is very difficult using MAR, which may drastically reduce the analysed frequency range. MAR may therefore lead to inaccurate standard deviation data. For polynomial detrending, the main disadvantage is the user-defined parameter of the polynomial order: a higher order may attenuate the lowest frequencies that can still be attributed to corrosion. In addition, it is difficult to select an optimal polynomial degree automatically. Therefore, considering the drawbacks of these traditionally used trend removal methods, wavelet analysis, a commonly used time-frequency method for trend removal [31], is chosen in this study. An eight-level discrete wavelet decomposition with a Daubechies 4 wavelet is reported to effectively remove the DC trend on the one hand, while maintaining the useful corrosion information on the other hand. [31,35,36]. In this work, all trend removal was performed using this method.

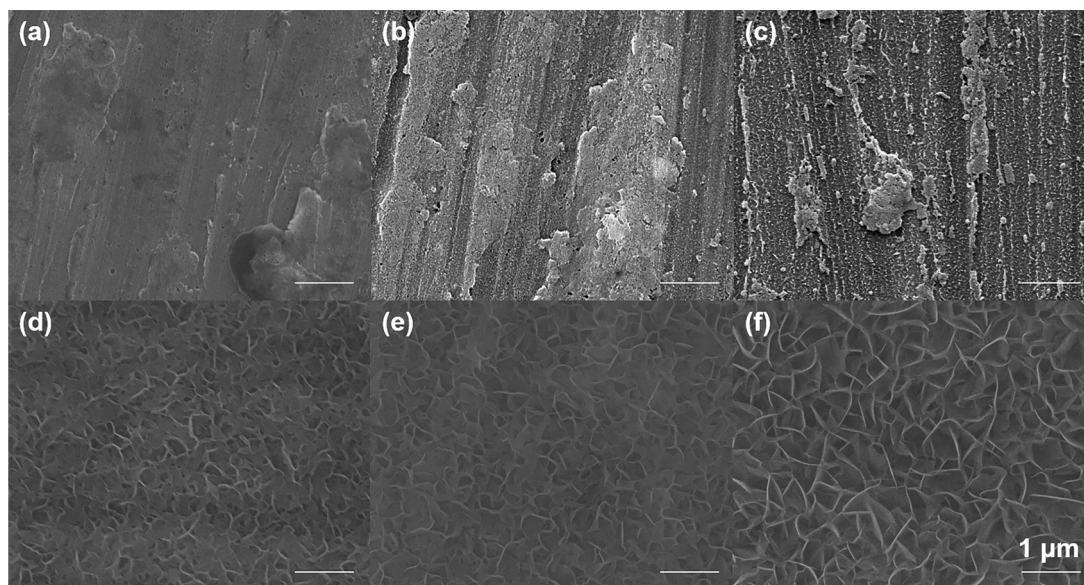


Fig. 3. Top-view SEM images of the AA2024-T3 surface exposed in 0.01 M NaCl and 0.01 M Li_2CO_3 at different exposure times: (a) 60 s; (b) 200 s; (c) 700 s; (d) 2000s; (e) 4000 s; (f) 14,500 s.

Noise resistance, defined as the ratio between the standard deviations of the potential and current fluctuations after trend removal, is expected to be close to the DC limit of the polarization resistance [37, 38]. In general, the time window for the calculation of standard deviations has a fixed size. If a moving time window which is shorter than the total recording time is employed, the noise resistance varies as a function of time.

As a mathematical tool, wavelets have been widely used to extract information from many different types of data, including e.g., audio signals and images [25]. In this paper, an analytic Morlet wavelet was used to generate the continuous wavelet transform (CWT) spectrum. A CWT spectrum simultaneously presents the energy distribution in the EN signal over time and frequency. For the CWT process, the signal was matched to a series of compressed or stretched versions of a wavelet by shifting the wavelet along the time axis. Compressing or stretching a wavelet is referred to as scaling, corresponding to the scaling parameter. Generally, CWT coefficient $C(a, b)$ is acquired by continuously varying the values of the scale parameter “a”, and the position parameter “b”. Scale parameter “a” corresponds to frequency and position parameter “b” denotes time. The amplitude, representing the local energy of the signal, is calculated and then plotted against scale parameter “a” and position parameter “b” to generate a time-frequency plot. Discrete wavelet transform (DWT) involves a similar process. The difference between CWT and DWT lies in the scaling factor and the time points. For the CWT, an arbitrary scaling factor is used and each scaled wavelet is shifted quasi-continuously along the time axis. However, the scaling factor for DWT is always two. In this way, DWT is more computation efficient. As a result, the CWT spectrum appears smoother as compared to an energy distribution plot from DWT [39].

2.3. Irreversibility and corrosion protection

The irreversibility properties and protectiveness of the lithium-based conversion layer were also assessed using EN. To generate a relatively uniform and compact conversion layer, hydrogen bubbles from the alkaline bath were removed by gently stirring the electrolyte every 10 min until no visible bubbles were left on the sample surfaces. After each initial exposure to the electrolyte, the solution was removed immediately. The exposed sample surface was rinsed gently using 0.01 M NaCl for 1 min to remove the residual lithium carbonate entirely. Then a volume of 0.321 μL 0.01 M NaCl solution was refilled to the

electrochemical cell. The reimmersion period also lasted for 14,500 s.

3. Results and discussion

3.1. EN data analysis and morphological characterization

The current and potential noise signals were recorded simultaneously as described in Section 2.1. Fig. 2a and b show the EN raw data obtained for the experiments on 0.01 M NaCl-0.01 M Li_2CO_3 (NaCl- Li_2CO_3) and 0.01 M NaCl-0.01 M Na_2CO_3 (NaCl- Na_2CO_3), respectively. The potential signals both exhibit a quick drop and then a gradual increase. In contrast, the current signals both present a large value with significant oscillations at the start which gradually reduce over time.

According to previous studies [14,22], steady passivation occurred during the alkaline bath immersion both in the NaCl- Li_2CO_3 and in the NaCl- Na_2CO_3 system. The passivation process can be divided into five different stages according to the potential variation. For the EN behavior of the AA2024-T3 sample exposed in NaCl- Li_2CO_3 solution, the potential has a sharp decrease to a minimum of -1408 mV during the first 60 s, accompanied by a relatively large current value of several microamperes (Stage I). Later, several potential increases follow. The first potential rise reaches a small plateau of -1225 mV at $t = 700$ s, where the current signal also presents a sharp alteration with small spikes (Stage II). The second potential rise reaches approximately -1000 mV at $t = 3000$ s, representing stage III. In this stage, the amplitudes of the current fluctuations gradually decay to a level of several tens of nanoamperes. The third rise in the potential is associated with stage IV, where potential values gradually reach up to -600 mV at $t = 5400$ s and the current values slightly decrease but are still in the same order of magnitude as the current fluctuations in stage III. Finally, the system reaches a relatively stable state where the potential slowly reaches up to -400 mV after an immersion period of 14500s. The current reaches a value of less than 10 nA (stage V).

Similarly, the signal variation of the AA2024-T3 sample exposed in NaCl- Na_2CO_3 electrolyte (Fig. 2b) presents a sharp initial potential decrease and four sequential potential rises as well. The potential initially drops to -1385 mV at $t = 80$ s (stage I) and then reaches a plateau value of -1170 mV at $t = 1400$ s (stage II). Stage III shows a stable potential at around -1170 mV, while the current signal fluctuates significantly. Stage IV starts at $t = 7200$ s with an “S” shape potential rise and ends when the potential reaches -240 mV at $t = 12000$ s. The

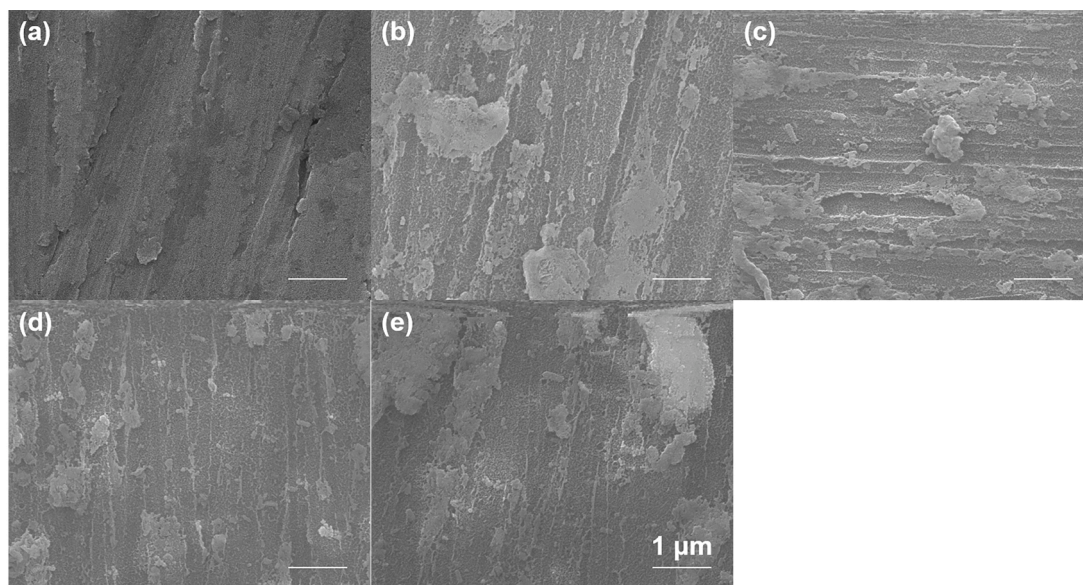


Fig. 4. Top-view SEM images of the AA2024-T3 surface exposed in 0.01 M NaCl and 0.01 M Na₂CO₃ at different exposure times: (a) 80 s; (b) 1400s; (c) 4000 s; (d) 10000s; (e) 14,500 s.

current value gradually decreases to a stable value of several tens of nanoamperes during this stage. During stage V, the system reaches a stable state where the potential slightly changes to -200 mV, while the current value does not present an obvious change as compared to the late fourth stage. According to the studies of Kosari et al. [22], local supersaturation of aluminate ions firstly occurs on the S-phase during the second stage, leading to the growth of a columnar-like conversion layer at the location of the S-phase in the existence of lithium ions. This local passivation explains why the potential value of the small plateau shown in Fig. 2a is slightly higher than that of Fig. 2b.

3.2. Morphological characterization

The surface of the samples was analysed by SEM at the different stages identified during the EN analysis. Fig. 3a–f show top-view SEM images of the AA2024-T3 surface after different periods of exposure to 0.01 M NaCl + 0.01 M Li₂CO₃ solution. The time intervals include $t = 60$ s (late first stage), $t = 200$ s (early second stage), $t = 700$ s (late second stage), $t = 2000$ s (third stage), $t = 4000$ s (fourth stage), and $t = 14500$ s (fifth stage). After the initial immersion period (Fig. 3a and b), a roughened morphology appears on the sample surface, indicating corrosion of the alloy matrix. The alloy surface experiences dissolution of the oxide film in the first stage, followed by dissolution of the aluminium matrix and dealloying of intermetallic particles at the second stage [22]. After 700 s (Fig. 3c), more severe corrosion is observed, but a columnar-like morphology starts to appear at the late second stage. The growing columnar outer layer explains the gradual decrease of the current signal at the third stage, since the protective layer gradually inhibits the diffusion of corrosive ions and the dissolution of the matrix. A clearer columnar structure is observed on the alloy surface after an exposure of 2000s (Fig. 3d). With increasing exposure time (Fig. 3e and f), the columnar outer layer keeps growing in harmony with a dense inner layer providing an enhanced corrosion protection [14]. This corresponds to the EN signals of Fig. 2a, which shows a diminishing EN current and a higher OCP.

Fig. 4a–e show SEM images for the exposure to 0.01 M NaCl + 0.01 M Na₂CO₃ solution at $t = 80$ s (late first stage), $t = 1400$ s (second stage), $t = 4000$ s (third stage), $t = 10000$ s (fourth stage), and $t = 14500$ s (fifth stage). In this case, a typical corrosion-attack morphology of the aluminium matrix in alkaline environments is present [40]. Irregular corrosion products cover an increasing number of locations at the

surface with immersion time. Although this corrosion product layer still inhibits the dissolution of the matrix to some extent, its protective effect is far less effective as compared to the lithium-containing conversion layer (shown in Fig. 2).

To avoid the interference of low-frequency energy and to focus on the transient signals appearing in the current signal, Fig. 5a and b show the raw data from 0 to 3000 s after trend removal for the samples exposed in NaCl-Li₂CO₃ and NaCl-Na₂CO₃ electrolyte, respectively (Detailed views of the timeframe between 600 s and 700 s of Fig. 5a and b are shown in Fig. 5a' and Fig. 5b', respectively).

In the presence of lithium ions, the current signal oscillations mainly appear in the first 1000s, followed by a relatively stable passive state. This indicates that localized electrochemical reactions mainly occur in the initial alkaline bath immersion period and that lithium ions are beneficial for the passivation and stabilization of the corroding surface of AA2024-T3. However, for the measurements without lithium ions, transient oscillations last considerably longer, which means that the corrosion process proceeds without effective suppression. The potential signals for both immersion conditions appear to exhibit nearly the same shape without noticeable oscillations, except for the first 100 s. Another interesting finding is that two types of transients appear, each with a distinct time span. The high frequency transients (type I) usually last no more than 0.5 s, while the duration of the intermediate frequency transients (type II) is usually in the order of several seconds. Both transient types correspond to different phenomena. This will be discussed in detail later.

As a statistical parameter, the value of the noise resistance is inversely proportional to the corrosion rate [29,38,41]. Fig. 6a and b show the variation of noise resistance as a function of time in the NaCl-Li₂CO₃ and NaCl-Na₂CO₃ solution, respectively. The calculated noise resistance values for the two different systems are both relatively smooth and low at the beginning, owing to the highly corrosive alkaline electrolytes. This is followed by an increasing trend, along with increasing fluctuation amplitudes. It is evident that the action of lithium ions increases the noise resistance of AA2024-T3. In addition, the increase of the noise resistance occurs earlier as compared to the case without lithium ions, indicating that surface passivation in the electrolyte containing lithium ions precedes the process of the benchmark group without lithium ions. This corresponds well with the morphological observations. The noise resistance in Fig. 6a is still relatively small at the early third stage, indicating that the sample surface is not

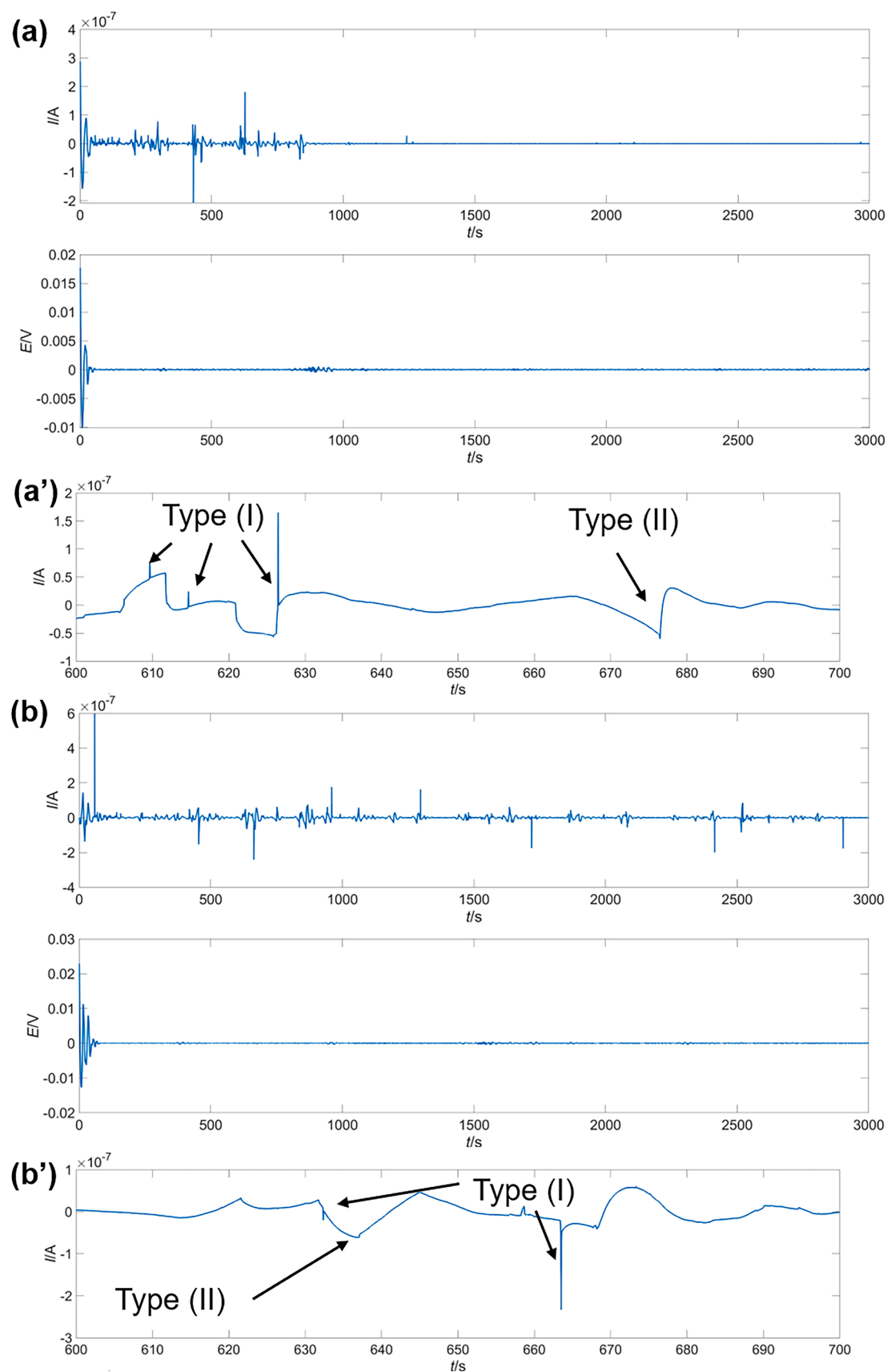


Fig. 5. EN current and potential signal after trend removal of samples exposed in (a) 0.01 M NaCl and 0.01 M Li_2CO_3 solution, and (b) 0.01 M NaCl and 0.01 M Na_2CO_3 solution for a duration of 3000 s. Fig. 5(a') and (b') Detailed views of the timeframes between 600 s and 700 s of Fig. 5(a) and (b), respectively.

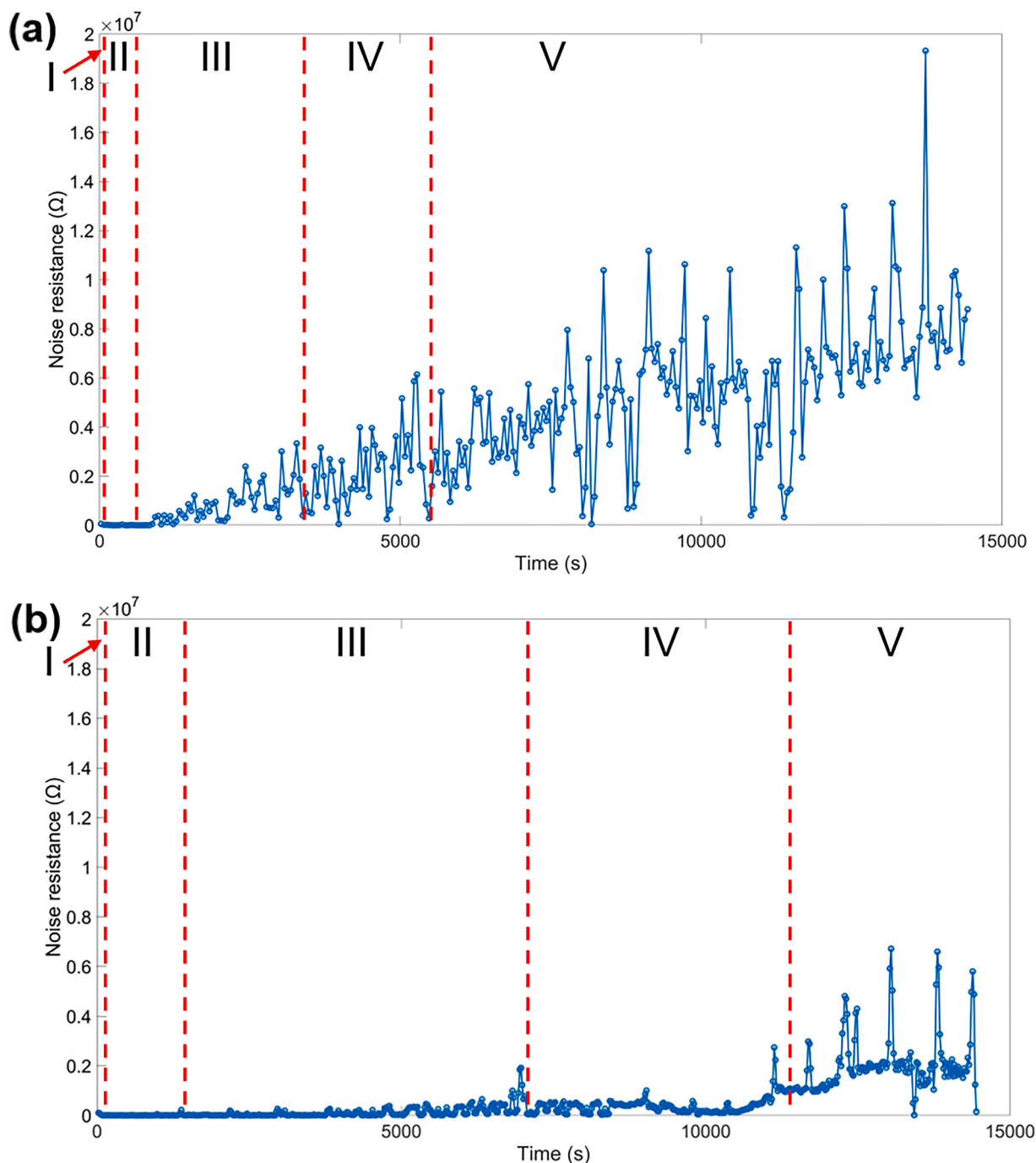


Fig. 6. Noise resistance calculated for AA2024-T3 electrodes immersed in (a) 0.01 M NaCl and 0.01 M Li_2CO_3 solution, and (b) 0.01 M NaCl and 0.01 M Na_2CO_3 solution for a duration of 14,500 s.

yet fully covered by the conversion layer. In this case, the columnar structure cannot fully inhibit the diffusion of corrosive electrolyte. With the growth of the columnar structure and the increasing coverage of the conversion layer, the noise resistance increases. The noise resistance in the fourth and fifth stages mainly indicates a passive state and full coverage of the conversion layer. The noise resistance steadily increases, but with more significant oscillations due to the competitive growth and dissolution of the substrate [8,14,22].

In order to study the temporal evolution and the dominant corrosion process simultaneously, Fig. 7a and b show the CWT spectrum of the EN current for AA2024-T3 samples exposed in NaCl- Li_2CO_3 and NaCl- Na_2CO_3 from 0 to 1500 s in the time-frequency domain and the corresponding optical images after an immersion period of 14500s,

respectively.

As shown in the spectra and indicated in red, most of the energy is concentrated in the low-frequency band, below 10^{-2} Hz. This is due to the fast uniform dissolution, which is typical for aluminium alloys that are exposed to highly corrosive alkaline electrolytes. Different local maxima are present in the high-frequency band, above 1 Hz, and are expected to be caused by the detachment of hydrogen bubbles from the AA2024-T3 surface. A fresh surface that was initially protected by the bubble is suddenly exposed to the corrosive solution, causing an increase of the exposed area. This leads to a sudden increase in the current. Video evidence for the bubble detachment and the corresponding high-frequency transient occurrence is shown in Movie S1 and Fig. S1. The number of high-frequency transients of samples exposed to NaCl-

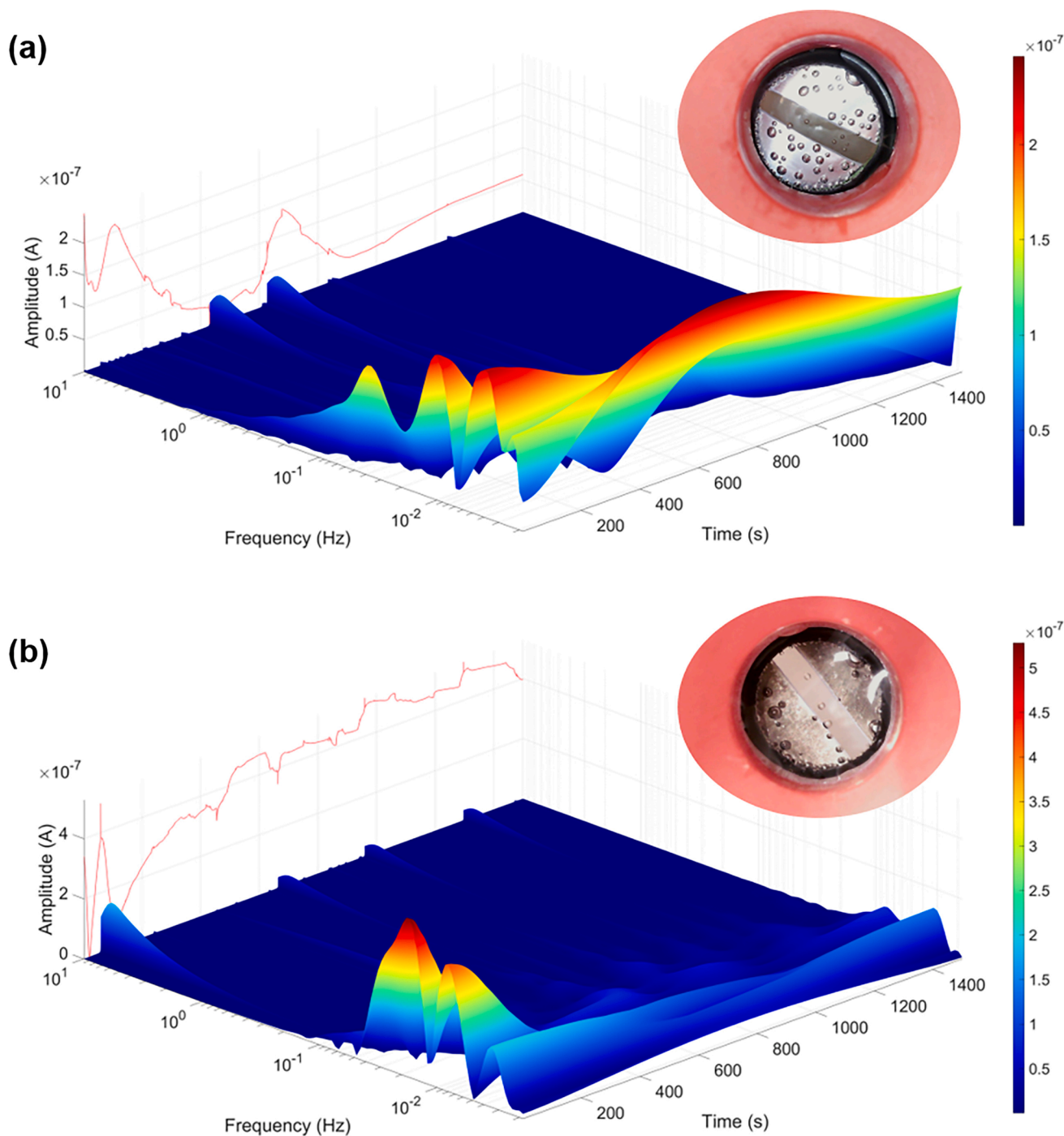


Fig. 7. CWT spectrum of the EN current for AA2024-T3 exposed in (a) 0.01 M NaCl and 0.01 M Li_2CO_3 solution, and (b) 0.01 M NaCl and 0.01 M Na_2CO_3 solution, from 0 to 1500 s.

Na_2CO_3 electrolyte is higher than that of samples exposed to NaCl- Li_2CO_3 , visible in Fig. 5. This indicates that more hydrogen bubbles detach in the absence of lithium ions. In addition, as shown in the corresponding optical figures, the quantitative difference in high-frequency transients is inversely proportional to the number of bubbles still present at the sample surface. This further proves that this type of high-frequency transients is related to the detachment of hydrogen bubbles. To avoid the interference of low-frequency energy and to make the transient signals appear more clearly, the EN current CWT spectra from Fig. 7 are plotted again in Fig. 8, after the removal of the low-frequency band using an eight-level Daubechies 4 wavelet. The first 100 s are omitted to avoid the interference of fast current variations due to the

instability of the samples immediately after exposure to highly corrosive electrolytes.

Two parallel electrochemical reactions with distinct frequencies are present, which corresponds well with the results in Fig. 5. For the samples exposed in NaCl- Li_2CO_3 solution, the amplitudes of these two reactions gradually decrease to zero in the early phase of the third stage (approximately 800 s). In contrast, the sample immersed in NaCl- Na_2CO_3 continuously exhibits two parallel electrochemical reactions. According to previous morphological and compositional studies on intermetallic particles of AA2024-T3, it is known that aluminium matrix dissolution, dealloying and copper enrichment of intermetallic particles are the dominant electrochemical reactions during the second stage and

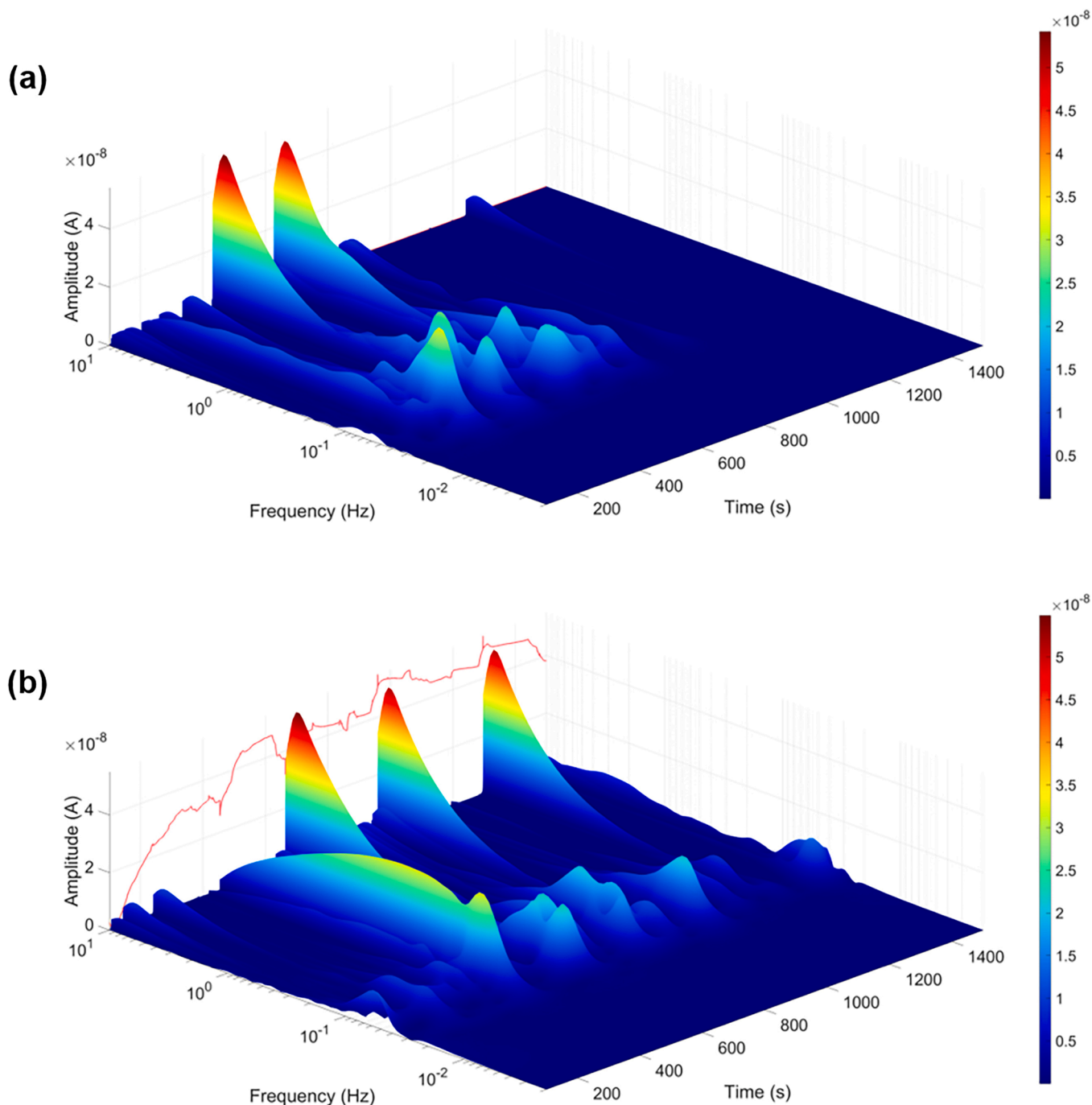


Fig. 8. CWT spectrum of the EN current after removal of the DC drift for AA2024-T3 exposed in (a) 0.01 M NaCl and 0.01 M Li_2CO_3 , and (b) 0.01 M NaCl and 0.01 M Na_2CO_3 , from 100 to 1500 s.

early third stage [22]. Therefore, the intermediate frequency range of the EN current signal can be attributed to the dealloying of intermetallic particles and micro-galvanic reactions between the aluminium matrix and (partially) dealloyed intermetallic particles [42]. For the purpose of verification, the CWT spectrum of pure Al from 100 to 1500 s is shown in Fig. S2. It is clear that high-frequency energy caused by hydrogen bubbles is still visible in the spectrum, whereas the amplitudes at intermediate frequencies are significantly lower.

3.3. Corrosion protection evaluation of the lithium-based conversion layer

Excellent irreversible corrosion-protective properties are an important indicator for the long-term protection of inhibitors [19]. In order to

verify this, the corrosion characteristics of AA2024-T3 that were previously exposed in a NaCl- Li_2CO_3 solution or a NaCl- Na_2CO_3 solution (further denoted as ‘treated’) are compared to bare AA2024-T3 (further denoted as ‘untreated’). Fig. 9a–c present the EN data for treated AA2024-T3 in NaCl- Li_2CO_3 solution and NaCl- Na_2CO_3 solution, and for untreated AA2024-T3, all three exposed in 0.01 M NaCl solution, respectively. Their corresponding top-view SEM observations are shown in Fig. 10.

For the treated sample in NaCl- Li_2CO_3 , the potential initially decreases to almost -1000 mV and then gradually increases to nearly -300 mV. The initial potential drop may be attributed to the release of the residue of carbonate ions that are incorporated into the columnar sublayer of the conversion layer or limited dissolution of the Li-

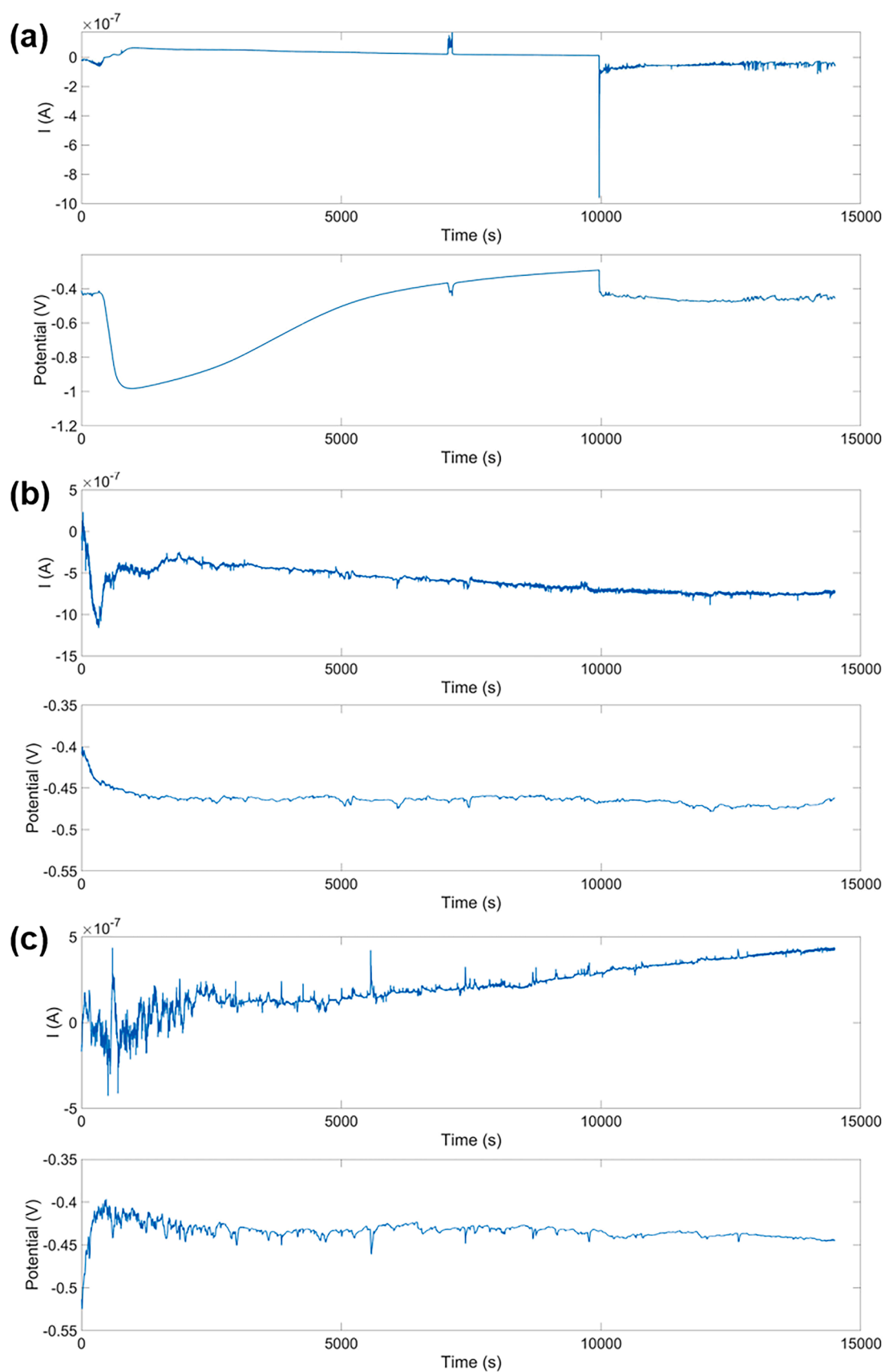


Fig. 9. EN current and potential signal for (a) AA2024-T3 treated in 0.01 M NaCl and 0.01 M Li_2CO_3 solution for 14500s, and (b) AA2024-T3 treated in 0.01 M NaCl and 0.01 M Na_2CO_3 solution for 14,500 s, and (c) untreated AA2024-T3 exposed in 0.01 M NaCl solution for 14,500 s.

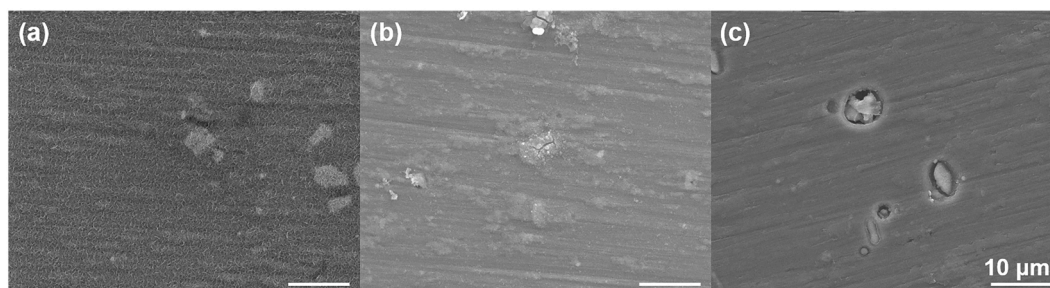


Fig. 10. Top-view SEM images of the AA2024-T3 surface (a) treated in a 0.01 M NaCl and 0.01 M Li_2CO_3 solution for 14,500 s, (b) treated in a 0.01 M NaCl and 0.01 M Na_2CO_3 solution for 14,500 s, and (c) untreated AA2024-T3 exposed in a 0.01 M NaCl solution for 14,500 s.

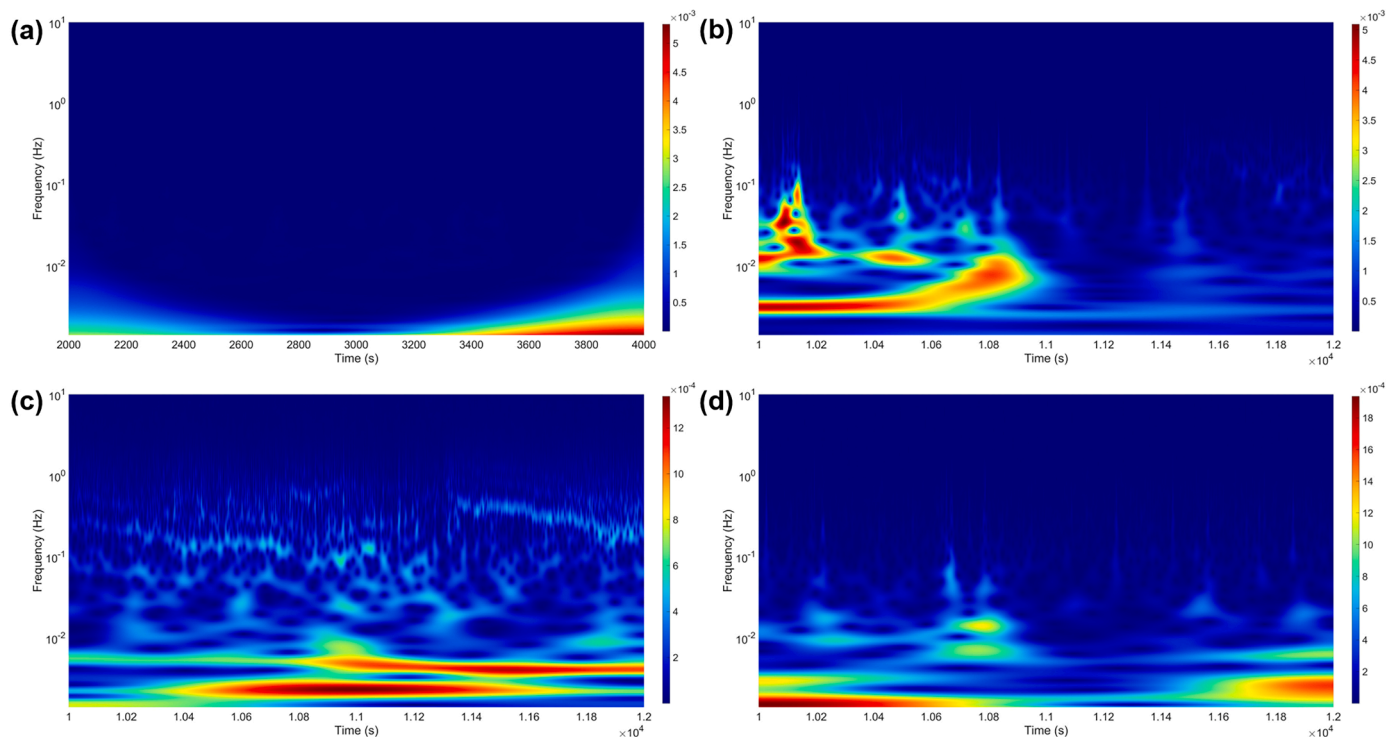


Fig. 11. CWT spectrum of the EN potential noise for AA2024-T3 treated in NaCl- Li_2CO_3 solution exposed in 0.01 M NaCl solution from (a) 2000 to 4000 s and (b) 10,000 to 12,000 s. CWT spectrum of the EN potential noise for AA2024-T3 treated in NaCl- Na_2CO_3 solution (c) and untreated AA2024-T3 (d) exposed in 0.01 M NaCl solution from 10,000 to 12,000 s.

intercalated LDH/pseudoboehmite, which causes a local alkaline environment. At a later stage, the potential gradually increases due to the consumption or dilution of carbonate ions. The pH variation during the re-immersion period also indicates that the solution turned into a weak alkaline condition with time (Fig. S4). Finally, an instantaneous potential drop occurs, after which the potential remains at a relatively stable value at around -450 mV. Similarly, the current signal exhibits an obvious passive state before the sudden potential drop, with negligible fluctuations and a low DC value. After this drop, the current abruptly increases and reaches a relatively stable value of approximately 50 nA. From Fig. 10a, obvious pitting cannot be observed. Corrosion activity after the breakdown of the conversion layer is likely to occur mainly underneath the outer columnar layer. For AA2024-T3 specimens treated in NaCl- Na_2CO_3 solution, the porous corrosion product layer cannot prevent the alloy surface from corrosion attack at all.

On the contrary, the porous layer even promotes further corrosion since the current signal shown in Fig. 9b shows an even higher net value than untreated AA2024-T3 shown in Fig. 9c. Cracks at certain locations are present under the formed corrosion products, indicating localised corrosion processes (Fig. 10b). For untreated AA2024-T3, the potential

initially increases due to the dealloying of intermetallic particles. This is followed by a copper enrichment and redistribution process [26,42]. At a later stage, the potential signal gradually stabilizes at around -440 mV, which is close to the potential value of the treated samples in NaCl- Li_2CO_3 after the sudden potential drop, and to the potential value of the treated samples in NaCl- Na_2CO_3 solution. From Fig. 10c, it is obvious that corrosion mainly occurs around intermetallic particles. Therefore, it can be concluded that the drastic potential drop results from the breakdown of the lithium-based conversion layer by chloride ions exposing the underlying AA2024-T3 substrate.

To investigate the difference in the time-frequency domain of samples with and without the protection of the lithium-based conversion layer, Fig. 11a–d present the CWT spectra of the EN potential noise for samples treated in NaCl- Li_2CO_3 solution within a timeframe of 2000 s before and after the breakdown, for samples treated in NaCl- Na_2CO_3 solution and for untreated AA2024-T3, respectively.

Treated AA2024-T3 samples in NaCl- Li_2CO_3 solution exhibit an obvious passive state from 2000 to 4000 s owing to the protection provided by the lithium-based conversion layer (Fig. 11a), while meta-stable and stable pitting events are observed after the drastic potential

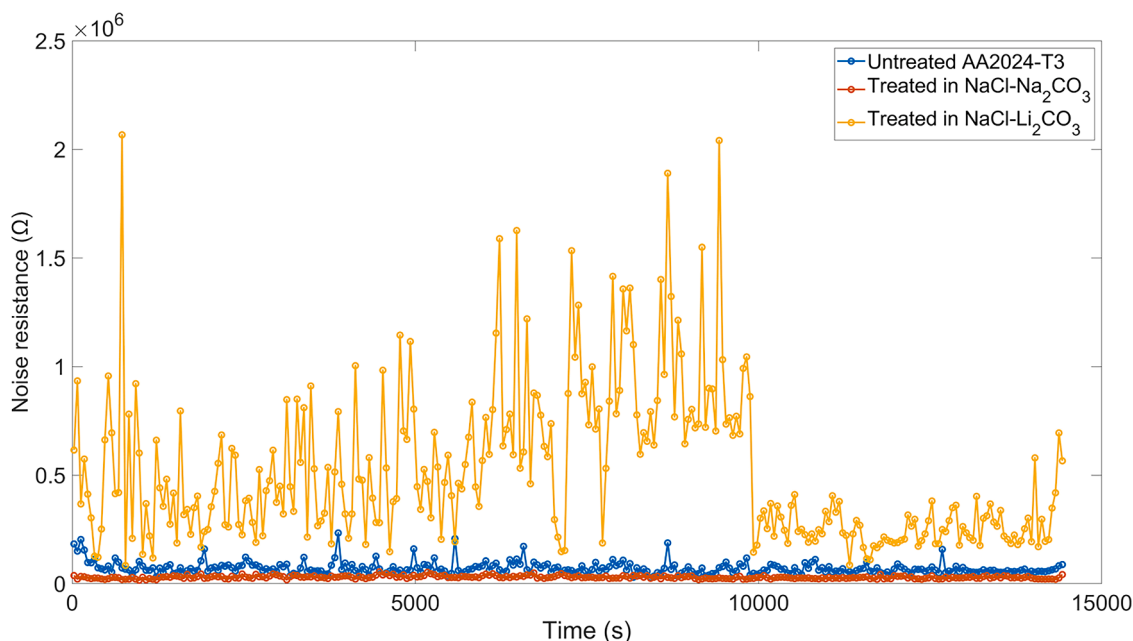


Fig. 12. Noise resistance calculated for AA2024-T3 treated in NaCl-Li₂CO₃ solution (yellow), in NaCl-Na₂CO₃ solution (red) and for untreated AA2024-T3 electrodes (blue), immersed in 0.01 M NaCl solution from 0 to 14,500 s.

drop between 10,000 and 12,000 s (Fig. 11b). This is caused by the local breakdown of the conversion layer by chlorides. However, for samples treated in NaCl-Na₂CO₃ (Fig. 11c) and untreated specimens (Fig. 11d), the dominant energy contribution in the CWT spectra is associated to stable pitting. In other words, the pitting corrosion process is less likely to stop once it is triggered by corrosive ions without the protection of the lithium-based conversion layer. This explanation also corresponds well to Fig. 10, since no obvious pitting is observed when the alloy surface is covered by the lithium-based conversion layer. Therefore, in the presence of the lithium-based conversion layer, even though localized corrosion occurs at the surface, there is a more significant change that a certain percentage of the pitting process is still suppressed by the conversion layer. This leads to a combination of metastable- and stable pitting corrosion.

Moreover, to quantitatively investigate the corrosion protection capability of the lithium-based conversion layer, Fig. 12 shows the noise resistance variation as a function of time of untreated AA2024-T3, treated AA2024-T3 in NaCl-Na₂CO₃ solution and NaCl-Li₂CO₃ solution.

As seen in Fig. 12, the noise resistance of the samples protected by the lithium-based conversion layer increases slightly over time before the breakdown, followed by a sudden drop, which remains at a relatively stable value. However, the resistance of the sample with the lithium-based conversion layer after the breakdown of the conversion layer is still nearly an order of magnitude larger than that of samples treated in NaCl-Na₂CO₃ and of untreated AA2024-T3 samples. This confirms that the lithium-based conversion layer is still able to provide corrosion protection to AA2024-T3, even while local conversion layer breakdown occurs.

4. Conclusions

Electrochemical noise has been proven to be a powerful technique to obtain *in-situ*, frequency- and time-resolved information about the lithium-based conversion layer formation mechanism and its robust protectiveness. The following conclusions were drawn:

- (a) The detachment of hydrogen bubbles, localized and uniform corrosion generate different features in the EN signals with

energy maxima in high, intermediate and low frequency bands, respectively;

- (b) Hydrogen evolution, trenching of the matrix and dealloying of intermetallic particles are dominant localized electrochemical reactions occurring simultaneously in the first two stages and in the early third stage. After that, the growth of a passive conversion layer is the dominant process;
- (c) Lithium ions favour the stabilization of corrosion products and significantly delay the corrosion degradation of AA2024-T3;
- (d) The lithium-based conversion layer is still protective after re-immersion in a NaCl containing electrolyte where lithium ions are absent, despite the local breakdown of the protective film.

CRediT authorship contribution statement

Ziyu Li: Visualization, Investigation, Formal analysis, Writing – original draft. **Axel Homborg:** Writing – review & editing, Investigation. **Yaiza Gonzalez-Garcia:** Writing – review & editing, Investigation. **Ali Kosari:** Writing – review & editing. **Peter Visser:** Writing – review & editing. **Arjan Mol:** Writing – review & editing, Investigation.

Declaration of Competing Interest

The authors declare no competing interests.

Data availability

Data will be made available on request.

Acknowledgement

The authors wish to acknowledge the financial support from the China Scholarship Council (CSC).

Supplementary materials

Supplementary material associated with this article can be found, in the online version, at [doi:10.1016/j.electacta.2022.140733](https://doi.org/10.1016/j.electacta.2022.140733).

References

- [1] A. Boag, R.J. Taylor, T.H. Muster, N. Goodman, D. McCulloch, C. Ryan, B. Rout, D. Jamieson, A.E. Hughes, Stable pit formation on AA2024-T3 in a NaCl environment, *Corros. Sci.* 52 (2010) 90–103.
- [2] N. Birbilis, Y.M. Zhu, S.K. Kairy, M.A. Glenn, J.F. Nie, A.J. Morton, Y. Gonzalez-Garcia, H. Terryn, J.M.C. Mol, A.E. Hughes, A closer look at constituent induced localised corrosion in Al-Cu-Mg alloys, *Corros. Sci.* 113 (2016) 160–171.
- [3] A. Kosari, F. Tichelaar, P. Visser, H. Zandbergen, H. Terryn, J.M.C. Mol, Dealloying-driven local corrosion by intermetallic constituent particles and dispersoids in aerospace aluminium alloys, *Corros. Sci.* 177 (2020), 108947.
- [4] R. Rosliza, W.B. Wan Nik, H.B. Senin, The effect of inhibitor on the corrosion of aluminum alloys in acidic solutions, *Mater. Chem. Phys.* 107 (2008) 281–288.
- [5] A.K. Mishra, R. Balasubramaniam, Corrosion inhibition of aluminum alloy AA 2014 by rare earth chlorides, *Corros. Sci.* 49 (2007) 1027–1044.
- [6] O. Gharbi, S. Thomas, C. Smith, N. Birbilis, Chromate replacement: what does the future hold? *NPJ Mater. Degrad.* 2 (2018) 12.
- [7] P. Santa Coloma, U. Izagirre, Y. Belaustegi, J.B. Jorcin, F.J. Cano, N. Lapeña, Chromium-free conversion coatings based on inorganic salts (Zr/Ti/Mn/Mo) for aluminum alloys used in aircraft applications, *Appl. Surf. Sci.* 345 (2015) 24–35.
- [8] P. Visser, Y. Liu, X. Zhou, T. Hashimoto, G.E. Thompson, S.B. Lyon, L.G.J. van der Ven, A.J.M.C. Mol, H.A. Terryn, The corrosion protection of AA2024-T3 aluminium alloy by leaching of lithium-containing salts from organic coatings, *Farad. Discuss.* 180 (2015) 511–526.
- [9] G. Bierwagen, R. Brown, D. Battocchi, S. Hayes, Active metal-based corrosion protective coating systems for aircraft requiring no-chromate pretreatment, *Prog. Org. Coat.* 67 (2010) 195–208.
- [10] M. Becker, Chromate-free chemical conversion coatings for aluminum alloys, *Corros. Rev.* 37 (2019) 321–342.
- [11] Y. Liu, P. Visser, X. Zhou, S.B. Lyon, T. Hashimoto, M. Curioni, A. Gholinia, G. E. Thompson, G. Smyth, S.R. Gibbon, D. Graham, J.M.C. Mol, H. Terryn, Protective film formation on AA2024-T3 aluminium alloy by leaching of lithium carbonate from an organic coating, *J. Electrochem. Soc.* 163 (2015) C45.
- [12] P. Visser, Y. Liu, H. Terryn, J.M.C. Mol, Lithium salts as leachable corrosion inhibitors and potential replacement for hexavalent chromium in organic coatings for the protection of aluminum alloys, *J. Coat. Technol. Res.* 13 (2016) 557–566.
- [13] P. Visser, A. Lutz, J.M.C. Mol, H. Terryn, Study of the formation of a protective layer in a defect from lithium-leaching organic coatings, *Prog. Org. Coat.* 99 (2016) 80–90.
- [14] P. Visser, Y. Gonzalez-Garcia, J.M.C. Mol, H. Terryn, Mechanism of passive layer formation on AA2024-T3 from alkaline lithium carbonate solutions in the presence of sodium chloride, *J. Electrochem. Soc.* 165 (2018) C60–C70.
- [15] P. Visser, H. Terryn, J.M.C. Mol, Active corrosion protection of various aluminium alloys by lithium-leaching coatings, *Surf. Interface Anal.* 51 (2019) 1276–1287.
- [16] J. Gui, T.M. Devine, Influence of lithium on the corrosion of aluminum, *Scr. Metall.* 21 (1987) 6. United States.
- [17] R.G. Buchheit, M.D. Bode, G.E. Stoner, Corrosion-resistant, chromate-free talc coatings for aluminum, *Corrosion* 50 (1994) 205–214.
- [18] P. Visser, S. A. Hayes, Anti-corrosive coating composition, WIP Organization (Ed.), WO 112605 (2010): A1.
- [19] P. Visser, H. Terryn, J.M.C. Mol, On the importance of irreversibility of corrosion inhibitors for active coating protection of AA2024-T3, *Corros. Sci.* 140 (2018) 272–285.
- [20] A. Kosari, P. Visser, F. Tichelaar, S. Eswara, J.N. Audinot, T. Wirtz, H. Zandbergen, H. Terryn, J.M.C. Mol, Cross-sectional characterization of the conversion layer formed on AA2024-T3 by a lithium-leaching coating, *Appl. Surf. Sci.* 512 (2020), 145665.
- [21] K. Marcoen, P. Visser, G.F. Trindade, M.L. Abel, J.F. Watts, J.M.C. Mol, H. Terryn, T. Hauffman, Compositional study of a corrosion protective layer formed by leachable lithium salts in a coating defect on AA2024-T3 aluminium alloys, *Prog. Org. Coat.* 119 (2018) 65–75.
- [22] A. Kosari, F. Tichelaar, P. Visser, H. Zandbergen, H. Terryn, J.M.C. Mol, Laterally-resolved formation mechanism of a lithium-based conversion layer at the matrix and intermetallic particles in aerospace aluminium alloys, *Corros. Sci.* 190 (2021), 109651.
- [23] P. Visser, M. Meeusen, Y. Gonzalez-Garcia, H. Terryn, J.M.C. Mol, Electrochemical evaluation of corrosion inhibiting layers formed in a defect from lithium-leaching organic coatings, *J. Electrochem. Soc.* 164 (2017) C396–C406.
- [24] A.M. Homborg, T. Tinga, E.P.M. van Westing, X. Zhang, G.M. Ferrari, J.H.W. de Wit, J.M.C. Mol, A critical appraisal of the interpretation of electrochemical noise for corrosion studies, *Corrosion* 70 (2014) 971–987.
- [25] D.-H. Xia, Y. Behnamian, Electrochemical noise: a review of experimental setup, instrumentation and DC removal, *Russ. J. Electrochem.* 51 (2015) 593–601.
- [26] A.M. Homborg, E.P.M. van Westing, T. Tinga, G.M. Ferrari, X. Zhang, J.H.W. de Wit, J.M.C. Mol, Application of transient analysis using Hilbert spectra of electrochemical noise to the identification of corrosion inhibition, *Electrochim. Acta* 116 (2014) 355–365.
- [27] P.J. Denissen, A.M. Homborg, S.J. Garcia, Interpreting electrochemical noise and monitoring local corrosion by means of highly resolved spatiotemporal real-time optics, *J. Electrochem. Soc.* 166 (2019) C3275–C3283.
- [28] D.H. Xia, S. Song, Y. Behnamian, W. Hu, Y.F. Cheng, J.L. Luo, F. Huet, Review-electrochemical noise applied in corrosion science: theoretical and mathematical models towards quantitative analysis, *J. Electrochem. Soc.* 167 (2020), 081507.
- [29] Y.J. Tan, S. Bailey, B. Kinsella, Studying the formation process of chromate conversion coatings on aluminium using continuous electrochemical noise resistance measurements, *Corros. Sci.* 44 (2002) 1277–1286.
- [30] X. Liu, T. Zhang, Y. Shao, G. Meng, F. Wang, *In-situ* study of the formation process of stannate conversion coatings on AZ91D magnesium alloy using electrochemical noise, *Corros. Sci.* 52 (2010) 892–900.
- [31] A.M. Homborg, T. Tinga, X. Zhang, E.P.M. van Westing, P.J. Oninckx, J.H.W. de Wit, J.M.C. Mol, Time-frequency methods for trend removal in electrochemical noise data, *Electrochim. Acta* 70 (2012) 199–209.
- [32] F. Mansfeld, Z. Sun, Technical note: localization index obtained from electrochemical noise analysis, *Corrosion* 55 (1999) 915–918.
- [33] F. Mansfeld, Z. Sun, C.H. Hsu, Electrochemical noise analysis (ENA) for active and passive systems in chloride media, *Electrochim. Acta* 46 (2001) 3651–3664.
- [34] U. Bertocci, F. Huet, R.P. Nogueira, P. Rousseau, Drift removal procedures in the analysis of electrochemical noise, *Corrosion* 58 (2002) 337–347.
- [35] I. Mohammadi, T. Shahabi, M. Mahdavian, M. Izadi, Sodium diethyldithiocarbamate as a novel corrosion inhibitor to mitigate corrosion of 2024-T3 aluminum alloy in 3.5 wt% NaCl solution, *J. Mol. Liq.* 307 (2020), 112965.
- [36] M.J. Bahrami, M. Shahidi, S.M.A. Hosseini, Comparison of electrochemical current noise signals arising from symmetrical and asymmetrical electrodes made of Al alloys at different pH values using statistical and wavelet analysis. Part I: neutral and acidic solutions, *Electrochim. Acta* 148 (2014) 127–144.
- [37] H. Ashassi-Sorkhabi, D. Seifzadeh, M.G. Hosseini, EN, EIS and polarization studies to evaluate the inhibition effect of 3H-phenothiazin-3-one, 7-dimethylamin on mild steel corrosion in 1M HCl solution, *Corros. Sci.* 50 (2008) 3363–3370.
- [38] R.A. Cottis, Interpretation of electrochemical noise data, *Corrosion* 57 (2001) 265–285.
- [39] R.A. Cottis, A.M. Homborg, J.M.C. Mol, The relationship between spectral and wavelet techniques for noise analysis, *Electrochim. Acta* 202 (2016) 277–287.
- [40] K.C. Emregül, A.A. Aksüt, The behavior of aluminum in alkaline media, *Corros. Sci.* 42 (2000) 2051–2067.
- [41] Y.J. Tan, S. Bailey, B. Kinsella, The monitoring of the formation and destruction of corrosion inhibitor films using electrochemical noise analysis (ENA), *Corros. Sci.* 38 (1996) 1681–1695.
- [42] A. Kosari, H. Zandbergen, F. Tichelaar, P. Visser, P. Taheri, H. Terryn, J.M.C. Mol, *In-situ* nanoscopic observations of dealloying-driven local corrosion from surface initiation to in-depth propagation, *Corros. Sci.* 177 (2020), 108912.